Improving high-order VEM stability on badly-shaped elements

Available online at www.sciencedirect.com
ScienceDirect
Mathematics and Computers in Simulation 216 (2024) 367–385
MATHEMATICS AND COMPUTERS IN SIMULATION
www.elsevier.com/locate/matcom

Original articles

Improving high-order VEM stability on badly-shaped elements

Stefano Berrone[1], Gioana Teora[*,1], Fabio Vicini[1]

Dipartimento di Scienze Matematiche, Politecnico di Torino, Corso Duca degli Abruzzi 24, 10129 Torino, Italy

Received 28 February 2023; received in revised form 3 August 2023; accepted 3 October 2023
Available online 9 October 2023

Abstract

For the 2D and 3D Virtual Element Methods, a new approach to improve the conditioning of local and global matrices in the presence of badly-shaped polytopes is proposed. This new method defines the local projectors and the local degrees of freedom with respect to a set of scaled monomials recomputed on more well-shaped polytopes. This new approach is less computationally demanding than using the orthonormal polynomial basis. The effectiveness of our procedure is tested on different numerical examples characterized by challenging geometries of increasing complexity.

Keywords: Ill-conditioning; Virtual element method; Polygonal mesh; Polyhedral mesh; Polynomial basis

1. Introduction

In recent years, numerical methods for the approximation of Partial Differential Equations (PDEs) on polygonal and polyhedral meshes, such as Virtual Element Methods (VEM) [3,4] or Hybrid High Order (HHO) methods [8] are gaining considerable interest since they offer a convenient framework to handle challenging geometries. In particular, the Virtual Element Method, introduced in [3] for the Poisson problem and then extended in [5] to general second-order elliptic problems with variable coefficients, is a generalization of the Finite Element Method (FEM), which includes suitable non-polynomial functions as well as the usual polynomial functions in the local space, to employ generic polytopal meshes and to build high-order methods. The use of these features is made possible by the introduction of suitable projection operators and by the careful selection of the local space and of local degrees of freedom (DOFs), which eliminate the need to compute in a closed form these non-polynomial functions. It is known from the VEM literature (see for example [6]) that the resulting system matrix is ill-conditioned in the presence of badly-shaped elements (collapsing bulks, small edges, etc.) when resorting to the scaled monomial basis in the definition of both the local projectors and the local DOFs.

In [6,7,10], it has been suggested to replace the scaled monomial basis with an orthonormal polynomial basis to cure ill-conditioning and make the VEM solution more reliable and accurate, but this strategy can be very expensive from a computational point of view. In this paper, we propose an alternative strategy to the use of an orthonormal polynomial basis in 2D and 3D, which is much less expensive and has already led to an improvement of global

* Corresponding author.
E-mail addresses: stefano.berrone@polito.it (S. Berrone), gioana.teora@polito.it (G. Teora), fabio.vicini@polito.it (F. Vicini).
[1] Member of INdAM research group GNCS.

https://doi.org/10.1016/j.matcom.2023.10.003

performances in the two-dimensional setting of HHO [9]. It consists of recomputing the scaled monomial basis on suitable polytopes whose inertia tensor is the identity tensor (re-scaled by a proper constant) and, thus of defining the local projectors and the local degrees of freedom as a function of such new polynomial basis to limit the condition numbers of local matrices and to improve global performances.

The structure of this work is as follows. In Section 2, we define the desired properties of a well-shaped polytope and we build an affine isomorphism that allows for transforming a generic polytope into a new one that has the requested features. In Section 3, we introduce the model problem and the VEM discretization on well-shaped polytopes. Finally, in Section 4, we propose some numerical experiments that show the advantages of using the new procedure with respect to the standard monomial basis or the orthonormal basis both in the two and three-dimensional cases.

Throughout this paper, we use the following notations. Given a polytope E, we denote by $h_E = \max_{\boldsymbol{x},\boldsymbol{y}\in E} \|\boldsymbol{x}-\boldsymbol{y}\|$, $\boldsymbol{x}_E$ and $|E|$ its diameter, centroid and measure (i.e. length or area or volume), respectively.

Let us denote by $\mathbb{P}^d_k(E)$ the set of the d-dimensional polynomials defined on E of degree less than or equal to $k \geq 0$ and by $n^d_k = \dim \mathbb{P}^d_k(E)$. For the ease of notation, we further set $\mathbb{P}^d_{-1}(E) = \{0\}$ and $n^d_{-1} = 0$ and we use the two natural functions $\ell_2 : \mathbb{N}^2 \leftrightarrow \mathbb{N}$ and $\ell_3 : \mathbb{N}^3 \leftrightarrow \mathbb{N}$ such that:

$$\begin{aligned} &(0,0) \leftrightarrow 1, \quad (1,0) \leftrightarrow 2, \quad (0,1) \leftrightarrow 3, \quad (2,0) \leftrightarrow 4, \dots \\ &(0,0,0) \leftrightarrow 1, \ (1,0,0) \leftrightarrow 2, \ (0,1,0) \leftrightarrow 3, \ (0,0,1) \leftrightarrow 4, \ (2,0,0) \leftrightarrow 5, \dots \end{aligned} \tag{1}$$

On each polytope E, we define the set of scaled monomials of degree less than or equal to k, with $k \geq 0$, as the set

$$\mathcal{M}^d_k(E) = \left\{ m^{k,d}_\alpha = \left(\frac{\boldsymbol{x}-\boldsymbol{x}_E}{h_E}\right)^{\boldsymbol{\alpha}} : \boldsymbol{\alpha} = \ell_d(\alpha) \in \mathbb{N}^d, \alpha = 1, \dots, n^d_k \right\},$$

which is a polynomial basis for $\mathbb{P}^d_k(E)$.

Finally, as usual, we use $(\cdot,\cdot)_w$ and $\|\cdot\|_w$ to indicate the inner product and the norm in the Lebesgue space $\mathrm{L}^2(w)$ on some open subset $\omega \subset \mathbb{R}^d$, respectively.

2. Well-shaped polytopes

Let $\Omega \subset \mathbb{R}^d$, with $d = 2, 3$, be an open bounded polytopal domain. We consider a sequence of decompositions $\{\mathcal{T}_h\}_h$ of Ω made up of polytopal elements E, where we fix, as usual, $h = \max_{E\in\mathcal{T}_h} h_E$. We further denote by N^E_v, $\mathcal{E}_{h,E}$ and N^E_e the number of vertices, the set of edges and the number of edges of $E \in \mathcal{T}_h$, respectively. In addition, if $d = 3$, $\mathcal{F}_{h,E}$ indicates the set of the $N^E_f = \#\mathcal{F}_{h,E}$ faces of the polyhedron $E \in \mathcal{T}_h$ and we set $\mathcal{F}_h = \cup_{E\in\mathcal{T}_h}\mathcal{F}_{h,E}$. Now, we assume there exists a positive constant $\eta \in (0, 1)$ independent of h such that the following mesh regularity assumptions hold true [1,5]:

- each element $E \in \mathcal{T}_h$ is star-shaped with respect to a ball of radius $\geq \eta h_E$;
- if $d = 3$, each face $f \in \mathcal{F}_h$ is star-shaped with respect to a ball of radius $\geq \eta h_f$;
- for each element $E \in \mathcal{T}_h$,
  - if $d = 2$, for each edge $e \in \mathcal{E}_{h,E}$, it holds $|e| \geq \eta h_E$;
  - if $d = 3$, for each face $f \in \mathcal{F}_{h,E}$, for each edge $e \in \mathcal{E}_{h,f}$, it holds $|e| \geq \eta h_f \geq \eta^2 h_E$.

The quality of an element E reflects the extent to which the element satisfies the previous assumptions [11,12]. Thus, when $\eta \to 1$, the element exhibits good quality. On the other hand, the element has poor quality when η is small.

Definition 1. An element is classified as *badly-shaped* when $\eta \to 0$.

Let us denote by $\mathbf{T}^E \in \mathbb{R}^{d\times d}$ the inertia tensor of E with respect to its centroid $\boldsymbol{x}_E$ and the x_i-axes with $i = 1, \dots, d$, whose entries are defined as

$$\mathbf{T}^E_{ss} = \sum_{\substack{i=1,\dots,d \\ i\neq s}} \int_E (x_i - (\boldsymbol{x}_E)_i)^2, \quad \forall s = 1, \dots, d,$$

and

$$\mathbf{T}^E_{ij} = -\int_E (x_i - (\boldsymbol{x}_E)_i)(x_j - (\boldsymbol{x}_E)_j), \quad \forall i, j = 1, \dots, d, \ i \neq j.$$

Firstly, we recall that the products of inertia, i.e. the extra-diagonal entries of $\mathbf{T}^E$, represent a measure of the imbalance in the mass distribution. Secondly, as in [2], we classify the polytope E as *isotropic* if its *anisotropic ratio* r^E is such that

$$r^E := \frac{\mu^E_{\max}}{\mu^E_{\min}} \approx 1.$$

where $\mu^E_{\max}$, $\mu^E_{\min}$ are the maximum and the minimum eigenvalue of $\mathbf{T}^E$, respectively.

Definition 2. We define a *well-shaped* polytope E as an isotropic element whose tensor of inertia $\mathbf{T}^E$ is a diagonal matrix.

We observe that, in the absence of hanging nodes, a well-shaped polytope for Definition 2 satisfies the mesh assumptions. Therefore, this polytope is a high quality element according to Definitions 1 and 2. On the other hand, in the presence of hanging nodes, Definition 2 allows, for instance, small edges that participate in forming hanging nodes. Thus, a well-shaped polytope for Definition 2 could be classified as a badly-shaped element according to Definition 1.

Finally, our goal is to define an affine isomorphism F_E for each element $E \in \mathcal{T}_h$ such that F_E^{-1} maps E into a well-shaped polytope $\hat{E}$ according to Definition 2.

2.1. The inertial mapping

Let us define the mass matrix related to E as

$$\mathbf{H}^E = \int_E (\boldsymbol{x} - \boldsymbol{x}_E)(\boldsymbol{x} - \boldsymbol{x}_E)^T \in \mathbb{R}^{d\times d}, \tag{2}$$

that is a symmetric positive-definite real matrix. We consider its spectral decomposition

$$\mathbf{H}^E = \mathbf{Q}^E \mathbf{\Lambda}^E \left(\mathbf{Q}^E\right)^T,$$

where $\mathbf{Q}^E \in \mathbb{R}^{d\times d}$ is the orthonormal matrix whose columns represent the eigenvectors of the mass matrix $\mathbf{H}^E$ and $\mathbf{\Lambda}^E$ is the diagonal matrix whose diagonal entries are the eigenvalues λ^E_i, $i = 1, \dots, d$ of $\mathbf{H}^E$. Now, we define a new element $\tilde{E}$ through the affine map

$$\tilde{\boldsymbol{x}} \mapsto \mathbf{B}^E (\boldsymbol{x} - \boldsymbol{x}_E), \tag{3}$$

where $\mathbf{B}^E = \sqrt{\lambda^E_{\max}}\sqrt{\left(\mathbf{\Lambda}^{\mathbf{E}}\right)^{-1}} \left(\mathbf{Q}^E\right)^T$ is invertible and such that $\left|\det \mathbf{B}^E\right| = \frac{\left(\lambda^E_{\max}\right)^{d/2}}{\sqrt{\prod_{i=1}^d \lambda^E_i}}$, $\lambda^E_{\max} = \max_{i=1,\dots,d} \lambda^E_i$. We note that the centroid of $\tilde{E}$ is $\tilde{\boldsymbol{x}}_{\tilde{E}} = \mathbf{0}$ and $\mathbf{T}^{\tilde{E}}$ is a diagonal matrix. Indeed,

$$\begin{aligned}
\mathbf{T}^{\tilde{E}}_{ij} &= -\int_{\tilde{E}} \tilde{x}_i \tilde{x}_j \\
&= -\left|\det \mathbf{B}^E\right| \mathbf{B}^E(i,:) \int_E (\boldsymbol{x} - \boldsymbol{x}_E)(\boldsymbol{x} - \boldsymbol{x}_E)^T \left(\mathbf{B}^E(j,:)\right)^T \\
&= -\left|\det \mathbf{B}^E\right| \mathbf{B}^E(i,:)\mathbf{H}^E \left(\mathbf{B}^E(j,:)\right)^T \\
&= -\lambda^E_{\max} \left|\det \mathbf{B}^E\right| \frac{\left(\mathbf{Q}^E(:,i)\right)^T}{\sqrt{\lambda^E_i}} \mathbf{Q}^E \mathbf{\Lambda}^E \left(\mathbf{Q}^E\right)^T \frac{\mathbf{Q}^E(:,j)}{\sqrt{\lambda^E_j}} \\
&= -\lambda^E_{\max} \left|\det \mathbf{B}^E\right| \left(\frac{\left(\mathbf{Q}^E(:,i)\right)^T}{\sqrt{\lambda^E_i}} \left(\mathbf{Q}^E\sqrt{\mathbf{\Lambda}^E}\right)\right) \left(\left(\mathbf{Q}^E\sqrt{\mathbf{\Lambda}^E}\right)^T \frac{\mathbf{Q}^E(:,j)}{\sqrt{\lambda^E_j}}\right) \\
&= -\lambda^E_{\max} \left|\det \mathbf{B}^E\right| \mathbf{e}_i^T \mathbf{e}_j = 0, \quad \forall i, j = 1, \dots, d \text{ s.t. } i \neq j,
\end{aligned}$$

Table 1
Examples of F_E mapping if $d = 2$.

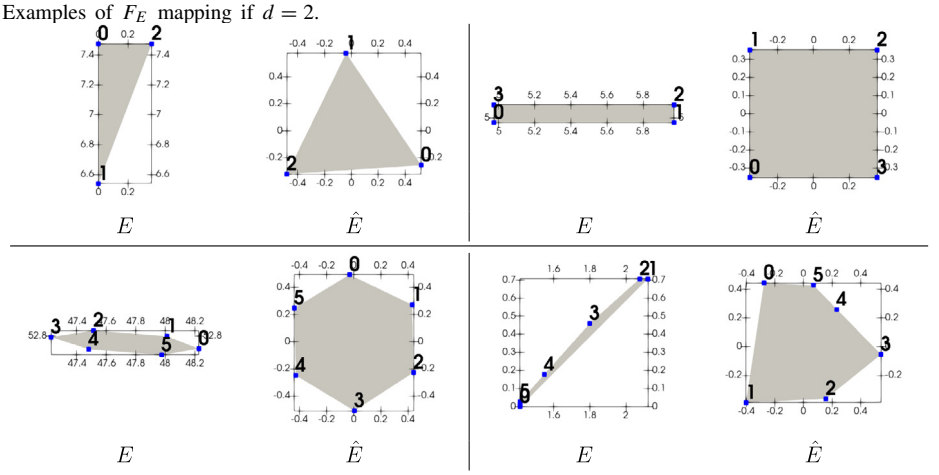

where, given a generic matrix $\mathbf{A}$, $\mathbf{A}(i,:)$ is the sub-matrix of $\mathbf{A}$ made up of its ith row, $\mathbf{A}(:,j)$ is the sub-matrix of $\mathbf{A}$ made up of its jth column and the set $\{\mathbf{e}_i\}_{i=1}^d$ represents the canonical basis of $\mathbb{R}^d$. Finally, concerning the diagonal entries of $\mathbf{T}^{\tilde{E}}$, we note that

$$\begin{aligned}\mathbf{T}^{\tilde{E}}_{ss} = \sum_{\substack{i=1,\dots,d\\ i\neq s}} \int_{\tilde{E}} \tilde{x}_i\tilde{x}_i &= \sum_{\substack{i=1,\dots,d\\ i\neq s}} \left|\det \mathbf{B}^E\right| \mathbf{B}^E(i,:)\mathbf{H}^E \left(\mathbf{B}^E(i,:)\right)^T \\ &= \sum_{\substack{i=1,\dots,d\\ i\neq s}} \lambda^E_{\max} \left|\det \mathbf{B}^E\right| \mathbf{e}_i^T\mathbf{e}_i \\ &= (d-1)\lambda^E_{\max}\left|\det \mathbf{B}^E\right|, \quad \forall s = 1,\dots,d.\end{aligned}$$

Thus, the diagonal entries prove to be constant with respect to the matrix index s. In conclusion, the new element $\tilde{E}$ is isotropic and well-shaped according to Definition 2.

We note that the computational cost of the mapping (3) depends only on the geometric dimension d of the problem but not on the order of accuracy of the discretization method. Furthermore, for stability reasons, it is preferable to perform a re-scaling before proceeding with this mapping to avoid small eigenvalues. Moreover, we also decide to re-scale elements after applying the mapping (3) to have polytopes with unit diameter.

In conclusion, on each element $E \in \mathcal{T}_h$, we perform sequentially the transformations

$$\begin{aligned} &E \longrightarrow \overline{E} \longrightarrow \tilde{E} \longrightarrow \hat{E} \\ &\boldsymbol{x} \mapsto \overline{\boldsymbol{x}} = \frac{1}{h_E}\boldsymbol{x} \mapsto \tilde{\boldsymbol{x}} = \mathbf{B}^{\overline{E}}\left(\overline{\boldsymbol{x}} - \overline{\boldsymbol{x}}_{\overline{E}}\right) \mapsto \hat{\boldsymbol{x}} = \frac{1}{h_{\tilde{E}}}\tilde{\boldsymbol{x}}.\end{aligned} \tag{4}$$

and we define the local mapping F_E such that

$$\boldsymbol{x} = F_E(\hat{\boldsymbol{x}}) = \boldsymbol{x}_E + \mathbf{F}^E\hat{\boldsymbol{x}}, \tag{5}$$

where

$$\mathbf{F}^E = h_E h_{\tilde{E}}\left(\mathbf{B}^{\overline{E}}\right)^{-1} \text{ and } \left|\det \mathbf{F}^E\right| = h_E^d h_{\tilde{E}}^d \left|\det\left(\mathbf{B}^{\overline{E}}\right)^{-1}\right|.$$

Examples of F_E mapping are shown in Tables 1 and 2 for the two-dimensional and the three-dimensional case, respectively.

Table 2
Examples of F_E mapping if $d = 3$.

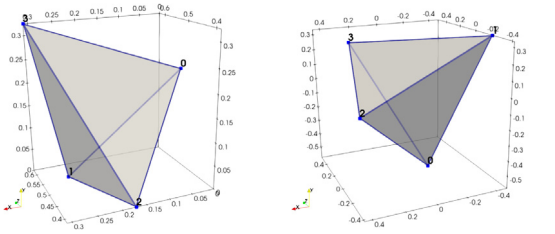

E $\hat{E}$

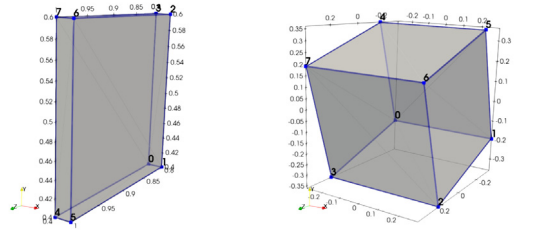

E $\hat{E}$

3. VEM discretization

Given $k \geq 1$, on each element $\hat{E} = F_E^{-1}(E)$ with $E \in \mathcal{T}_h$, we introduce the local projection operators $\hat{\Pi}_k^{\hat{\nabla},\hat{E}} : H^1(\hat{E}) \to \mathbb{P}_k^d\left(\hat{E}\right)$ and $\hat{\Pi}_k^{0,\hat{E}} : \mathrm{L}^2(\hat{E}) \to \mathbb{P}_k^d\left(\hat{E}\right)$, as

$$\begin{cases} \left(\hat{\nabla}\hat{p}, \hat{\nabla}\left(\hat{\Pi}_k^{\hat{\nabla},\hat{E}}\hat{v} - \hat{v}\right)\right)_{\hat{E}} = 0, \quad \forall \hat{p} \in \mathbb{P}_k^d\left(\hat{E}\right) \\ \hat{P}_0\left(\hat{\Pi}_k^{\hat{\nabla},\hat{E}}\hat{v} - \hat{v}\right) = 0, \end{cases} \tag{6}$$

and

$$\left(\hat{p}, \left(\hat{\Pi}_k^{0,\hat{E}}\hat{v} - \hat{v}\right)\right)_{\hat{E}} = 0, \quad \forall \hat{p} \in \mathbb{P}_k^d\left(\hat{E}\right), \tag{7}$$

where

$$\hat{P}_0(\hat{v}) = \begin{cases} (\hat{v}, 1)_{\partial\hat{E}} & \text{if } k = 1, \\ (\hat{v}, 1)_{\hat{E}} & \text{if } k > 1. \end{cases} \tag{8}$$

Furthermore, for the sake of convenience, we use the symbol $\hat{\Pi}_{k-1}^{0,\hat{E}}$ also for the L^2-projection operator of vector-valued functions onto the polynomial space $\left(\mathbb{P}_{k-1}^d\left(\hat{E}\right)\right)^2$, meaning a component-wise application.

If $d = 3$, we need to compute both the 3D projectors on E and the 2D projectors on each face $f \in \mathcal{F}_{h,E}$, thus we need to define a polynomial basis for $\mathbb{P}_k^3(E)$, $\forall E \in \mathcal{T}_h$, and a polynomial basis for $\mathbb{P}_k^2(f)$, $\forall f \in \mathcal{F}_h$, as highlighted in [4]. For this reason, we build three different approaches ((B), (F) and (B-F)) by defining, $\forall E \in \mathcal{T}_h$,

(B) the 3D set of scaled monomials on the well-shaped polyhedron $\hat{E} = F_E^{-1}(E)$ and the 2D sets of scaled monomials on the original faces $f \in \mathcal{F}_{h,E}$;

(F) the 3D set of scaled monomials on the original polyhedron E and the 2D sets of scaled monomials on the mapped faces $\check{f}$ obtained by applying a mapping F_f^{-1} to each face $f \in \mathcal{F}_{h,E}$ defined according to what is done for the two-dimensional case in Section 2.1;

(B-F) the 3D set of scaled monomials on $\hat{E} = F_E^{-1}(E)$ and the 2D sets of scaled monomials on the mapped faces $\check{f} = F_f^{-1}(f)$ for each $f \in \mathcal{F}_{h,E}$.

We want to highlight that in the (B-F) approach the new polygons $\check{f}$ are obtained by applying F_f^{-1} to the original faces f of E and not to faces $\hat{f}$ of $\hat{E}$. In the following, for the sake of convenience, we define F_f, $\forall f \in \mathcal{F}_h$, in the (B) approach and F_E, $\forall E \in \mathcal{T}_h$, in the (F) approach as the identity maps.

Now, on each $E \in \mathcal{T}_h$, following [1,5], we introduce the local enhanced Virtual Element spaces:

- if $d = 2$,

$$V_k^2(E) = \Big\{ v \in H^1(E) : \Delta v \in \mathbb{P}_k^2(E)\,,\ v_{|e} \in \mathbb{P}_k^1(e)\ \ \forall e \in \mathcal{E}_{h,E},\ v_{|\partial E} \in C^0(\partial E),$$
$$\left(\hat{v}, \hat{p}\right)_{\hat{E}} = \left(\hat{\Pi}_k^{\hat{\nabla},\hat{E}} \hat{v}, \hat{p}\right)_{\hat{E}}\ \ \forall \hat{p} \in \mathbb{P}_k^2\left(\hat{E}\right) \setminus \mathbb{P}_{k-2}^2\left(\hat{E}\right) \Big\};$$

- if $d = 3$,

$$V_k^3(E) = \Big\{ v \in H^1(E) : \Delta v \in \mathbb{P}_k^3(E)\,,\ v_{|f} \in V_k^2(f)\ \forall f \in \mathcal{F}_{h,E},\ v_{|\partial E} \in C^0(\partial E),$$
$$\left(\hat{v}, \hat{p}\right)_{\hat{E}} = \left(\hat{\Pi}_k^{\hat{\nabla},\hat{E}} \hat{v}, \hat{p}\right)_{\hat{E}}\ \ \forall \hat{p} \in \mathbb{P}_k^3\left(\hat{E}\right) \setminus \mathbb{P}_{k-2}^3\left(\hat{E}\right) \Big\},$$

where the set $\mathbb{P}_k^d\left(\hat{E}\right) \setminus \mathbb{P}_{k-2}^d\left(\hat{E}\right)$ denotes the set of polynomials of degree exactly k or $k-1$, $\hat{w}(\hat{\boldsymbol{x}}) = w(\boldsymbol{x}_E + \mathbf{F}^E \hat{\boldsymbol{x}})$ and $\nabla w = \left(\mathbf{F}^E\right)^{-T} \hat{\nabla} \hat{w}$, $\forall w \in V_k^d(E)$. We further define the following set of local DOFs: $\forall v_h \in V_k^d(\hat{E})$

1. the value of v_h at the vertices of E;
2. if $k > 1$, for each edge $e \in \mathcal{E}_{h,E}$, the value of v_h at the $k-1$ internal Gauss–Lobatto quadrature nodes on e;
3. if $k > 1$ and $d = 3$, for each face $f \in \mathcal{F}_{h,E}$, the scaled moments on $\check{f} = F_f^{-1}(f)$

$$\frac{1}{|\check{f}|} \left(\check{v}_h, \check{m}_\alpha^{k-2,d-1}\right)_{\check{f}}, \quad \forall \check{m}_\alpha^{k-2,d-1} \in \mathcal{M}_{k-2}^{d-1}\left(\check{f}\right); \tag{9}$$

4. if $k > 1$, the scaled moments on $\hat{E} = F_E^{-1}(E)$

$$\frac{1}{|\hat{E}|} \left(\hat{v}_h, \hat{m}_\alpha^{k-2,d}\right)_{\hat{E}}, \quad \forall \hat{m}_\alpha^{k-2,d} \in \mathcal{M}_{k-2}^{d}\left(\hat{E}\right). \tag{10}$$

Let $N_E^{\text{dof}} = \dim V_k^d(E)$, for each element $E \in \mathcal{T}_h$, we denote by dof_i^E the operator that associates its ith local degree of freedom to each sufficiently smooth function φ and by $\{\varphi_i\}_{i=1}^{N_E^{\text{dof}}}$ the set of local Lagrangian VEM basis functions related to the defined DOFs. Furthermore, we introduce the local projection matrices $\hat{\mathbf{\Pi}}_{\mathbf{k}}^{\hat{\nabla},\hat{\mathbf{E}}} \in \mathbb{R}^{n_k^d \times N_E^{\text{dof}}}$, $\hat{\mathbf{\Pi}}_{\mathbf{k-1}}^{\mathbf{0},\hat{\mathbf{E}}} \in \mathbb{R}^{n_{k-1}^d \times N_E^{\text{dof}}}$ and $\hat{\mathbf{\Pi}}_{\mathbf{k-1}}^{\mathbf{0},\hat{\mathbf{x}}_\mathbf{j},\hat{\mathbf{E}}} \in \mathbb{R}^{n_{k-1}^d \times N_E^{\text{dof}}}$, for $j = 1, \dots, d$, which are defined as

$$\begin{aligned} \hat{\Pi}_k^{\hat{\nabla},\hat{E}} \varphi_i &= \sum_{\alpha=1}^{n_k^d} \left(\hat{\mathbf{\Pi}}_{\mathbf{k}}^{\hat{\nabla},\hat{\mathbf{E}}}\right)_{\alpha i} \hat{m}_\alpha^{k,d}, \quad \hat{\Pi}_{k-1}^{0,\hat{E}} \varphi_i = \sum_{\alpha=1}^{n_{k-1}^d} \left(\hat{\mathbf{\Pi}}_{\mathbf{k-1}}^{\mathbf{0},\hat{\mathbf{E}}}\right)_{\alpha i} \hat{m}_\alpha^{k-1,d}, \\ \hat{\Pi}_{k-1}^{0,\hat{E}} \frac{\partial \varphi_i}{\partial \hat{x}_j} &= \sum_{\alpha=1}^{n_{k-1}^d} \left(\hat{\mathbf{\Pi}}_{\mathbf{k-1}}^{\mathbf{0},\hat{\mathbf{x}}_\mathbf{j},\hat{\mathbf{E}}}\right)_{\alpha i} \hat{m}_\alpha^{k-1,d}, \ \ \forall j = 1, \dots, d. \end{aligned} \tag{11}$$

We note that the definition of local DOFs makes the computation of the local projection matrices (11) completely independent of the geometric properties of the original element E in the two-dimensional case. On the other hand, in the three-dimensional case, the geometric properties of the original element E influence the computation of the projectors with an intensity that depends on the chosen approach ((B), (F) or (B-F)).

Finally, we introduce the global Virtual Element space

$$V_{h,k} = \left\{ v \in C^0\left(\overline{\Omega}\right) \cap H_0^1(\Omega) :\ v \in V_k^d(E)\ \ \forall E \in \mathcal{T}_h \right\}.$$

and, in agreement with the local choice of the DOFs, we define the following set of DOFs: $\forall v \in V_{h,k}$

1. the value of v_h at the internal vertices of the decomposition $\mathcal{T}_h$;
2. if $k > 1$, for each internal edge $e \in \mathcal{E}_h$, the value of v_h at the $k-1$ internal Gauss–Lobatto quadrature nodes on e;

3. if $k > 1$ and $d = 3$, for each internal face $f \in \mathcal{F}_h$, the scaled moments on $\check{f} = F_f^{-1}(f)$

$$\frac{1}{|\check{f}|}\left(\check{v}_h, \check{m}_\alpha^{k-2,d-1}\right)_{\check{f}}, \quad \forall \check{m}_\alpha^{k-2,d-1} \in \mathcal{M}_{k-2}^{d-1}\left(\check{f}\right); \tag{12}$$

4. if $k > 1$, for each element $E \in \mathcal{T}_h$, the scaled moments on $\hat{E} = F_E^{-1}(E)$

$$\frac{1}{|\hat{E}|}\left(\hat{v}_h, \hat{m}_\alpha^{k-2,d}\right)_{\hat{E}}, \quad \forall \hat{m}_\alpha^{k-2,d} \in \mathcal{M}_{k-2}^{d}\left(\hat{E}\right). \tag{13}$$

Remark 3.1. It is very important to set out monomials on the original faces and not on the faces of the mapped element $F_E^{-1}(E)$ to uniquely define the degrees of freedom (12) in the approach (B). For the same reason, in the approach (B-F), we apply the map F_f to the original faces f and not to faces $\hat{f}$ belonging to the mapped elements.

3.1. Example: an advection–diffusion–reaction problem

Let $\boldsymbol{D}$ be a symmetric uniformly positive definite tensor over Ω, $\gamma \geq 0$ be a sufficiently smooth function $\Omega \to \mathbb{R}$ and $\mathbf{b}$ be a smooth vector-valued function $\Omega \to \mathbb{R}^d$ s.t. $\nabla \cdot \mathbf{b} = 0$. Given $f \in \mathrm{L}^2(\Omega)$, we consider the following advection–diffusion–reaction problem

$$\begin{cases} -\nabla \cdot (\boldsymbol{D}\nabla u) + \mathbf{b} \cdot \nabla u + \gamma u = f & \text{in } \Omega \\ u = 0 & \text{on } \partial\Omega. \end{cases} \tag{14}$$

Without loss of generality, we assume homogeneous boundary Dirichlet conditions. The non-homogeneous case can be treated with the standard lifting procedure.

Now, $\forall E \in \mathcal{T}_h$, we introduce the local bilinear form

$$a^E(u, v) = \int_E \boldsymbol{D}\nabla u \cdot \nabla v + \int_E \mathbf{b} \cdot \nabla u v + \int_E \gamma u v$$

and we write the variational formulation of (14) as: *Find* $u \in V = H_0^1(\Omega)$ *such that*

$$\sum_{E \in \mathcal{T}_h} a^E(u, v) = \sum_{E \in \mathcal{T}_h} \int_E f v, \quad \forall v \in V. \tag{15}$$

We note that

$$\int_E (\boldsymbol{D}\nabla u) \cdot \nabla v = \int_{\hat{E}} \left(\hat{\nabla}\hat{u}\right)^T \left(\mathbf{F}^E\right)^{-1} \hat{\boldsymbol{D}} \left(\mathbf{F}^E\right)^{-T} \hat{\nabla}\hat{v} \left|\det \mathbf{F}^E\right|, \tag{16}$$

$$\int_E \mathbf{b} \cdot \nabla u v = \int_{\hat{E}} \hat{\mathbf{b}}^T \left(\mathbf{F}^E\right)^{-T} \hat{\nabla}\hat{u}\hat{v} \left|\det \mathbf{F}^E\right|,$$

$$\int_E \gamma u v = \int_{\hat{E}} \hat{\gamma}\hat{u}\hat{v} \left|\det \mathbf{F}^E\right|, \quad \int_E f v = \int_{\hat{E}} \hat{f}\hat{v} \left|\det \mathbf{F}^E\right|.$$

where, for all $\hat{\boldsymbol{x}} \in \hat{E}$,

$$\hat{\boldsymbol{D}}(\hat{\boldsymbol{x}}) = \boldsymbol{D}(\boldsymbol{x}_E + \mathbf{F}^E\hat{\boldsymbol{x}}), \quad \hat{\mathbf{b}}(\hat{\boldsymbol{x}}) = \mathbf{b}(\boldsymbol{x}_E + \mathbf{F}^E\hat{\boldsymbol{x}}),$$

$$\hat{\gamma}(\hat{\boldsymbol{x}}) = \gamma(\boldsymbol{x}_E + \mathbf{F}^E\hat{\boldsymbol{x}}), \quad \hat{f}(\hat{\boldsymbol{x}}) = f(\boldsymbol{x}_E + \mathbf{F}^E\hat{\boldsymbol{x}}).$$

Let us introduce on each element E the symmetric uniformly positive-definite tensor $\hat{\boldsymbol{\mathcal{K}}} = \left|\det \mathbf{F}^E\right| \left(\mathbf{F}^E\right)^{-1} \hat{\boldsymbol{D}} \left(\mathbf{F}^E\right)^{-T}$, the vector-valued function $\hat{\boldsymbol{\beta}} = \left|\det \mathbf{F}^E\right| \left(\mathbf{F}^E\right)^{-1} \hat{\mathbf{b}}$ and $\hat{\rho} = \left|\det \mathbf{F}^E\right| \hat{\gamma}$. We define the local virtual bilinear form as: $\forall u_h, v_h \in V_{h,k}$,

$$a_h^E(u_h, v_h) = \int_{\hat{E}} \left(\hat{\boldsymbol{\mathcal{K}}} \hat{\Pi}_{k-1}^{0,\hat{E}} \hat{\nabla}\hat{u}_h\right) \cdot \hat{\Pi}_{k-1}^{0,\hat{E}} \hat{\nabla}\hat{v}_h + C_{\boldsymbol{D}} S^E\left((I - \hat{\Pi}_k^{\hat{\nabla},\hat{E}})\hat{u}_h, (I - \hat{\Pi}_k^{\hat{\nabla},\hat{E}})\hat{v}_h\right)$$

$$+ \int_{\hat{E}} \hat{\boldsymbol{\beta}} \cdot \hat{\Pi}^{0,\hat{E}}_{k-1} \hat{\nabla} \hat{u}_h \; \hat{\Pi}^{0}_{k-1} \hat{v}_h$$
$$+ \int_{\hat{E}} \hat{\rho} \; \hat{\Pi}^{0,\hat{E}}_{k-1} \hat{u}_h \; \hat{\Pi}^{0,\hat{E}}_{k-1} \hat{v}_h,$$

where $C_{\boldsymbol{D}}$ is a constant depending on $\boldsymbol{D}$ and $S^E(\cdot,\cdot)$ is the standard *dofi–dofi* stabilization, i.e.

$$S^E(u_h, v_h) = h_E^{d-2} \sum_{i=1}^{N_E^{\mathrm{dof}}} \mathrm{dof}_i^E\left(\hat{u}_h\right) \mathrm{dof}_i^E\left(\hat{v}_h\right). \tag{17}$$

We note that it is very important to use the diameter h_E of the original element in Eq. (17) in order to scale $S^E(\cdot,\cdot)$ as $a^E(\cdot,\cdot)$. See [3] for further details.

Finally, the VEM discrete counterpart of (15) reads: *Find* $u_h \in V_{h,k}$ *such that*

$$\sum_{E\in\mathcal{T}_h} a_h^E(u_h, v_h) = \sum_{E\in\mathcal{T}_h} \int_{\hat{E}} \hat{f} \; \hat{\Pi}^{0,\hat{E}}_{k-1} \hat{v}_h \left|\det \mathbf{F}^E\right|, \quad \forall v_h \in V_{h,k}. \tag{18}$$

4. Numerical experiments

In this section, we propose some numerical experiments to validate the aforementioned approaches, which we generically call *inertial* (*Inrt* in short), in the two and three-dimensional cases. To show the advantages of using our procedures, we compare their performances in different discretizations of increasing complexity with respect to

- the standard monomial approach (*Mon* in short) described in [4];
- the orthonormal approach (*Ortho*, in short) which follows the construction presented in [7,10] for the two and three-dimensional cases, respectively. We highlight that for the three-dimensional case, we choose to use an orthonormal basis both in the bulks and on the faces of the decomposition.

In the following, for the ease of notation, we assume to work on mapped elements also in the monomial and in the orthonormal approaches, where the used maps F_E, $\forall E \in \mathcal{T}_h$, and F_f, $\forall f \in \mathcal{F}_h$, are the identity maps.

The comparison is based on the analysis of the condition numbers of local projection matrices that are defined in (11) and that are used to assemble the local system matrix. For the 3D case, we also analyse the condition numbers of the 2D local projection matrices $\check{\mathbf{\Pi}}^{\check{\nabla},\check{\mathbf{f}}}_{\mathbf{k}} \in \mathbb{R}^{n_k^d \times N_f^{\mathrm{dof}}}$, $\check{\mathbf{\Pi}}^{\mathbf{0},\check{\mathbf{f}}}_{\mathbf{k-1}} \in \mathbb{R}^{n_{k-1}^d \times N_f^{\mathrm{dof}}}$ that are employed for computing the boundary integrals appearing in the computation of the 3D local projection matrices. For the sake of brevity, we omit to report the behaviours of the condition number of the local projection matrices $\hat{\mathbf{\Pi}}^{\mathbf{0},\hat{\mathbf{E}}}_{\mathbf{k-1}}$ and $\check{\mathbf{\Pi}}^{\mathbf{0},\check{\mathbf{f}}}_{\mathbf{k-1}}$ since they do not add further information with respect to the others. Furthermore, we analyse the behaviours of the condition number of the global system matrix $\mathbf{A}$ of the discrete problem (18) and of the following relative error norms:

$$u^2_{\mathrm{err}} = \frac{\displaystyle\sum_{E\in\mathcal{T}_h} \int_{\hat{E}} \left(\hat{u} - \hat{\Pi}^{0,\hat{E}}_k \hat{u}_h\right)^2 \left|\det \mathbf{F}^E\right|}{\displaystyle\sum_{E\in\mathcal{T}_h} \|u\|^2_E}, \tag{19}$$

$$\nabla u^2_{\mathrm{err}} = \frac{\displaystyle\sum_{E\in\mathcal{T}_h} \int_{\hat{E}} \left(\hat{\nabla}\hat{u} - \hat{\Pi}^{0,\hat{E}}_{k-1} \hat{\nabla}\hat{u}_h\right)^T \left(\mathbf{F}^E\right)^{-1} \left(\mathbf{F}^E\right)^{-T} \left(\hat{\nabla}\hat{u} - \hat{\Pi}^{0,\hat{E}}_{k-1} \hat{\nabla}\hat{u}_h\right) \left|\det \mathbf{F}^E\right|}{\displaystyle\sum_{E\in\mathcal{T}_h} \|\nabla u\|^2_E}, \tag{20}$$

as the local polynomial degree k increases while keeping the mesh fixed.

We expect an overall improvement with respect to the monomial approach, but not necessarily with respect to the orthonormal approach. We emphasize that this work aims to propose a computationally cheap strategy to mitigate the ill-conditioning caused by using the standard scaled monomial basis defined on the original polytopal elements. In this regard, we recall that the additional cost of the orthonormal approach relies on the cost of the application of the Modified Gram Schmidt algorithm with reorthogonalization on each element (and on each face, if $d = 3$), which depends on $n_k^d = \frac{(k+1)\ldots(k+d)}{d!}$. On the other hand, the computational complexity of our method only depends

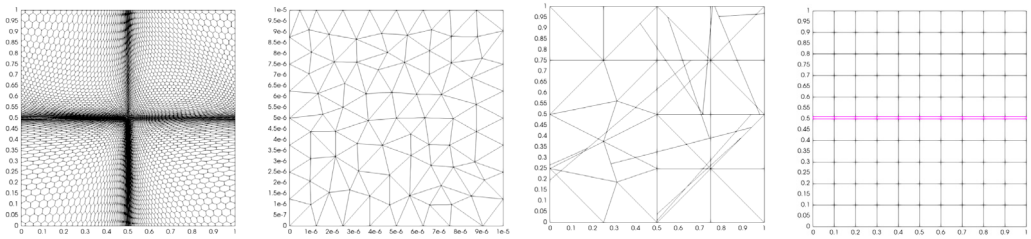

(a) (b) (c) (d)

Fig. 1. Meshes used for tests 1 and 2. Highly-distorted hexagonal mesh (HDHM) on 1(a). Triangular mesh on a small domain (RTRM) on 1(b). Polygonal mesh (GPGM) on 1(c). Collapsing polygons (CSM_1) on 1(d).

Table 3
Properties of meshes used in tests 1, 2 and 5.

	$\#\mathcal{T}_h$	N_v^E		Area			Diameter			Anisotropic ratio			Edge ratio		
		avg		min	avg	max	min	avg	max	min	avg	max	min	avg	max
HDHM	5711	5.9	E	2.6e−6	1.8e−4	1.3e−3	2.1e−3	2.4e−2	6.2e−2	1.0e+0	5.9e+1	6.2e+2	1.0e+0	2.5e+0	2.0e+1
			$\hat{E}$	5.0e−1	6.4e−1	6.5e−1	1.0e+0	1.0e+0	1.0e+0	1.0e+0	1.0e+0	1.0e+0	1.0e+0	1.1e+0	2.0e+0
RTRM	153	3	E	3.0e−13	6.5e−13	1.0e−12	1.0e−6	1.4e−6	1.9e−6	1.0e+0	2.3e+0	9.9e+0	1.0e+0	1.3e+0	2.8e+0
			$\hat{E}$	4.3e−1	4.3e−1	4.3e−1	1.0e+0	1.0e+0	1.0e+0	1.0e+0	1.0e+0	1.0e+0	1.0e+0	1.0e+0	1.0e+0
GPGM	81	4.3	E	3.7e−6	1.2e−2	3.1e−2	3.7e−3	2.0e−1	3.5e−1	1.3e+0	2.7e+1	4.7e+2	1.2e+0	5.1e+2	4.0e+4
			$\hat{E}$	4.3e−1	4.5e−1	5.3e−1	1.0e+0	1.0e+0	1.0e+0	1.0e+0	1.0e+0	1.0e+0	1.0e+0	1.3e+2	9.0e+3
CSM_1	110	4	E	1.0e−3	9.1e−3	1.0e−2	1.0e−1	1.4e−1	1.4e−1	1.0e+0	1.0e+1	1.0e+2	1.0e+0	1.8e+0	1.0e+1
			$\hat{E}$	5.0e−1	5.0e−1	5.0e−1	1.0e+0	1.0e+0	1.0e+0	1.0e+0	1.0e+0	1.0e+0	1.0e+0	1.0e+0	1.0e+0
CSM_2	110	4	E	1.0e−4	9.1e−3	1.0e−2	1.0e−1	1.4e−1	1.4e−1	1.0e+0	9.1e+2	1.0e+4	1.0e+0	1.0e+1	1.0e+2
			$\hat{E}$	5.0e−1	5.0e−1	5.0e−1	1.0e+0	1.0e+0	1.0e+0	1.0e+0	1.0e+0	1.0e+0	1.0e+0	1.0e+0	1.0e+0
CSM_3	110	4	E	1.0e−5	9.1e−3	1.0e−2	1.0e−1	1.4e−1	1.4e−1	1.0e+0	9.1e+4	1.0e+6	1.0e+0	9.2e+1	1.0e+3
			$\hat{E}$	5.0e−1	5.0e−1	5.0e−1	1.0e+0	1.0e+0	1.0e+0	1.0e+0	1.0e+0	1.0e+0	1.0e+0	1.0e+0	1.0e+0
CM	1072	3.4	E	2.7e−4	9.3e−4	5.0e−3	6.5e−2	1.4e−1	3.4e−1	1.9e+1	1.5e+2	7.7e+2	1.5e+0	5.6e+0	2.2e+1
			$\hat{E}$	3.1e−1	4.4e−1	6.2e−1	1.0e+0	1.0e+0	1.0e+0	1.0e+0	1.0e+0	1.0e+0	1.0e+0	1.1e+0	3.0e+1

on the geometric dimension d of the problem and, if $d = 3$, on the number of faces for the (F) and (B-F) inertial approaches, but not on the local polynomial degree k.

4.1. Test 1: Highly-distorted mesh, small domain and hanging nodes in 2D

Given $\epsilon \in \mathbb{R}^+$ and $\Omega = (0, \epsilon) \times (0, \epsilon)$, we consider the problem (14) with constant coefficients $\boldsymbol{D} = \mathbf{I}$, $\gamma = 0$ and $\mathbf{b} = \begin{bmatrix} 0 \\ 0 \end{bmatrix}$, where f and the non-homogeneous Dirichlet boundary condition are set in such a way the exact solution is:

$$u(x_1, x_2) = 1.1 + \frac{16}{\epsilon^4} x_1 x_2 (\epsilon - x_1)(\epsilon - x_2). \tag{21}$$

In this first test, we consider

- a highly-distorted hexagonal mesh (HDHM in short) on a square domain with edge length $\epsilon = 1$ (Fig. 1(a));
- a regular triangular mesh (RTRM in short) on a small square domain with edge length $\epsilon = 1.0e{-}5$ (Fig. 1(b));
- a generic polygonal mesh (GPGM in short) on a square domain with edge length $\epsilon = 1$, which is characterized by polygons with very different shapes and areas and by the presence of hanging nodes (Fig. 1(c)).

In Table 3, we show the main features of both the original and the mapped polygons related to each aforementioned mesh, namely the area, the diameter, the anisotropic ratio and the *edge ratio*, i.e. the ratio between

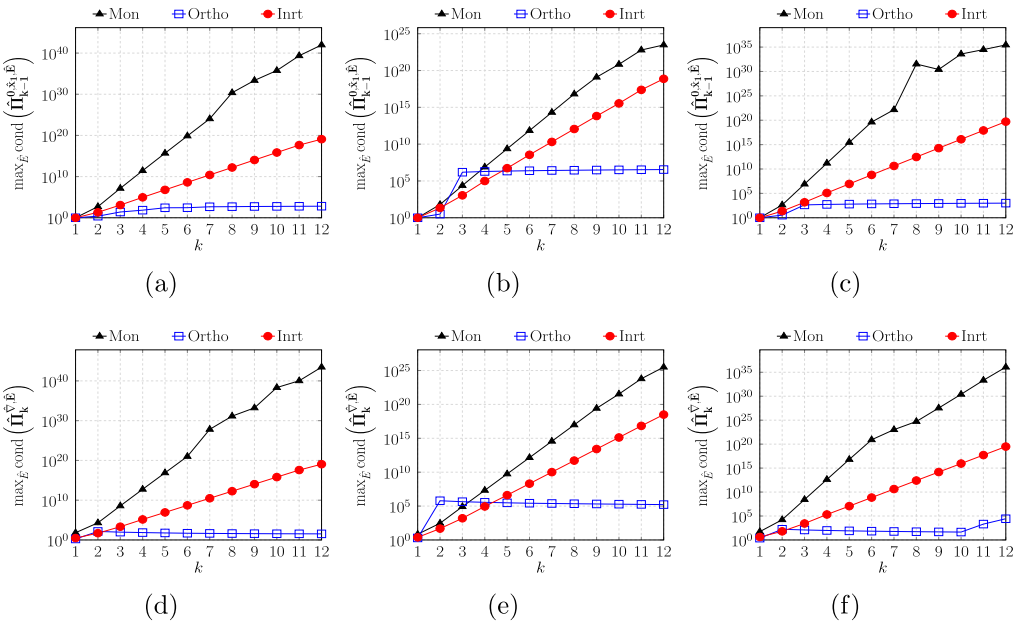

Fig. 2. Test 1: Behaviours of the worst condition numbers of local projection matrices among elements with respect to k. Left: HDHM. Centre: RTRM. Right: GPGM.

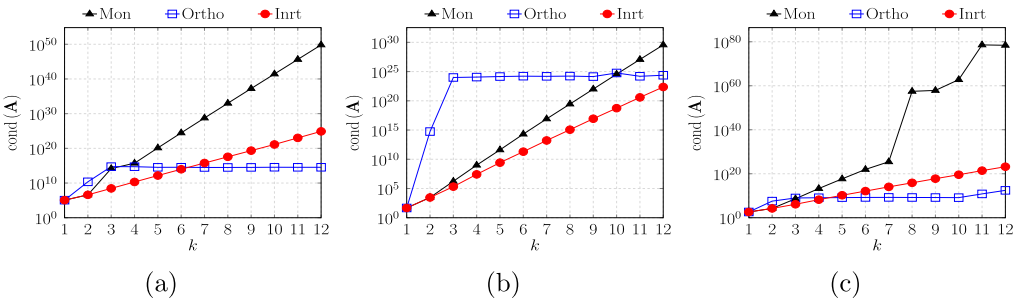

Fig. 3. Test 1: Behaviour of the condition number of the system matrix $\mathbf{A}$ with respect to k. Left: HDHM. Centre: RTRM. Right: GPGM.

the highest and the smallest lengths of edges of E. By looking at the geometric properties of $\hat{E}$, we note that the map F_E generates well-shaped polygons according to Definition 2. Furthermore, it tends to uniform the geometric properties of elements belonging to the same category (such as triangles, parallelograms, hexagons, etc.) in the absence of almost-hanging nodes, i.e. nodes between two consecutive edges forming an angle of about 180 degrees. Indeed, in the presence of almost-hanging nodes, our map does not eliminate any problems related to small edges that participate to form almost-hanging nodes, as highlighted by looking at the edge ratio property of the mesh GPGM.

In Figs. 2, 3 and 4, we show the trends of the condition numbers of the local projection matrices, of the global system matrix and of the errors (19)–(20) while varying the polynomial degree k, respectively. We omit the plots of the condition numbers of $\hat{\mathbf{\Pi}}^{\mathbf{0},\hat{\mathbf{x}}_2,\hat{\mathbf{E}}}_{\mathbf{k-1}}$ with respect to k, since its trend is very similar to the one of the condition number of $\hat{\mathbf{\Pi}}^{\mathbf{0},\hat{\mathbf{x}}_1,\hat{\mathbf{E}}}_{\mathbf{k-1}}$ for each method. In all the figures, we note that the inertial procedure outperforms the monomial one as expected.

In Fig. 2, we observe good local results of the inertial approach, although the best performances are obtained by the orthonormal approach for high values of k. In this regard, we remark that our aim is to cheaply reduce the ill-conditioning of local and global matrices in the presence of badly-shaped elements with respect to the monomial approach.

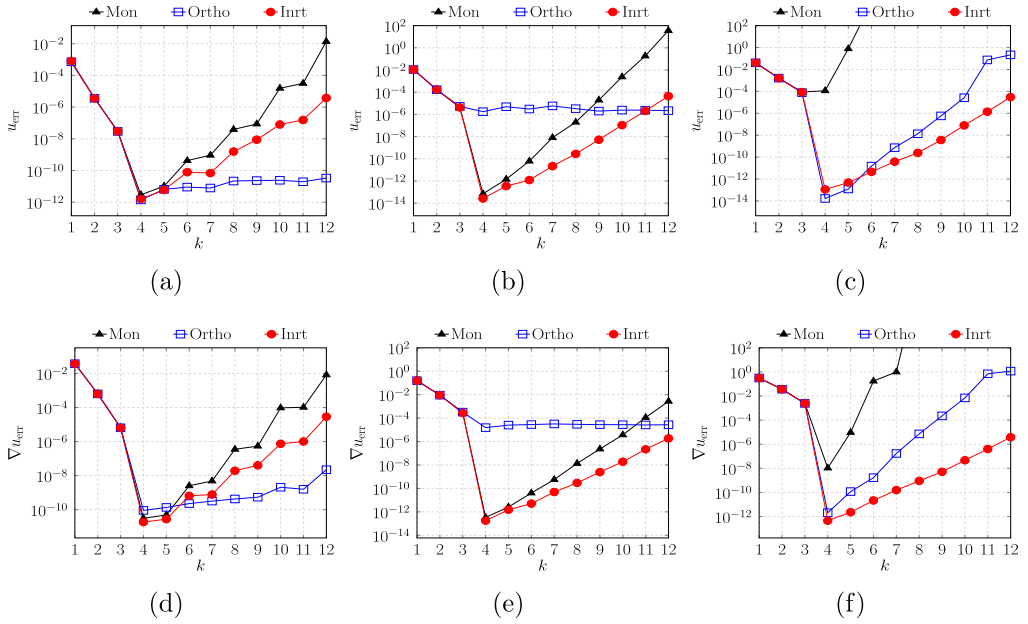

Fig. 4. Test 1: Behaviours of errors (19) and (20) with respect to k. Left: HDHM. Centre: RTRM. Right: GPGM.

We stress that, in the case of mesh RTRM, the first re-scaling in (4) is required for the Inrt approach. Indeed, the mass matrix related to the original RTRM elements is a singular matrix in finite precision due to its eigenvalues which are in the order of magnitude of the round-off error. We point out that the small triangles of RTRM represent a challenging geometry for the orthonormal approach. The inertial approach, instead, is robust in the presence of the small polygons of mesh RTRM in terms of the condition number of the global matrix (see Fig. 3(b)).

In the presence of very badly-shaped polygons of mesh GPGM, the global performances of the Ortho and Inrt methods are comparable (see Fig. 3(c)).

Since the proposed solution (21) is a polynomial of degree 4, we expect that the errors shown in Fig. 4 tend to zero when $k < 4$ and then vanish when $k \geq 4$. However, after an initial decrease, in most cases the errors start to raise due to the ill-conditioning. In this regard, we note that the monomial errors blow up in the case of mesh GPGM, while the growth of errors related to Inrt is much more controlled. Finally, we remark that the robustness of our method in the cases of RTRM and GPGM meshes is reflected in the smallest errors for the higher values of k, as highlighted in Figs. 4(b), 4(c), 4(e) and 4(f).

4.2. Test 2: Collapsing polygons

In this experiment, we test the performances of our procedures considering the complete diffusion–advection–reaction problem (14) with variable coefficients and a non-polynomial solution in the case of collapsing polygons. Thus, given $\Omega = (0, 1) \times (0, 1)$, we consider

$$\boldsymbol{D}(x_1, x_2) = \begin{bmatrix} 1 + x_2^2 & -x_1 x_2 \\ -x_1 x_2 & 1 + x_1^2 \end{bmatrix}, \quad \mathbf{b}(x_1, x_2) = \begin{bmatrix} x_1 \\ -x_2 \end{bmatrix}, \quad \gamma(x_1, x_2) = x_1 x_2,$$

and we set f in such a way the exact solution is

$$u(x_1, x_2) = \sin(\pi x_1) \sin(\pi x_2).$$

We generate a sequence of three rectangular meshes composed of squared elements of area 10^{-1} with the exception of a central band made up of two groups of rectangles, one of which (the purple band highlighted in Fig. 1(d)) is formed by rectangles of height 10^{-2}, 10^{-3} and 10^{-4} for CSM_1, CSM_2 and CSM_3, respectively. We refer to Fig. 1(d) for the plot of the first mesh CSM_1.

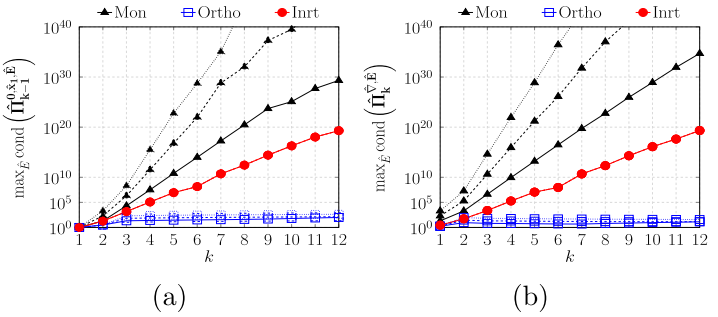

Fig. 5. Test 2: Behaviours of the worst condition numbers of local projection matrices among elements with respect to k. Solid lines: CSM_1. Dashed lines: CSM_2. Dotted lines: CSM_3.

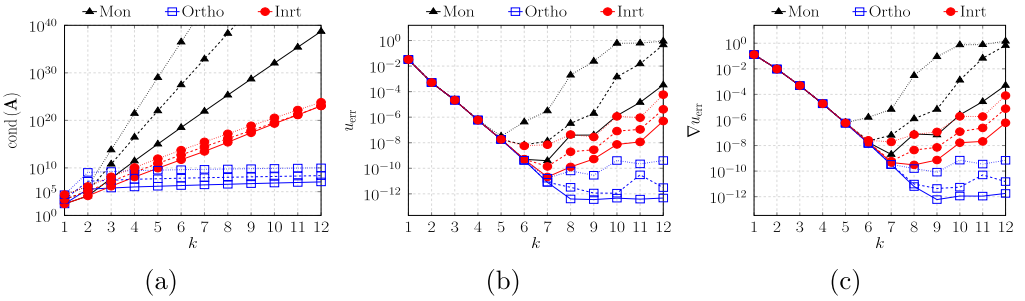

Fig. 6. Test 2: Behaviours of the condition numbers of the global system matrix and of errors (19), (20) with respect to k. Solid lines: CSM_1. Dashed lines: CSM_2. Dotted lines: CSM_3.

The geometric properties of the original and of the mapped elements of the three meshes are shown in Table 3 on the rows CSM_i, $i \in \{1, 2, 3\}$. We note that the performed map makes the mapped elements belonging to the central band equal to the other mapped ones. This result is well highlighted by looking at the condition numbers of local projection matrices in Fig. 5, which do not vary among the three meshes in the inertial approach. On the other hand, from the condition number of the global system matrix and from the error measurements shown in Fig. 6, we can observe that the global performances remain dependent of the geometric properties of the original elements also in the inertial approach. As done for Test 1, we omit to report the behaviours of the condition numbers of $\hat{\mathbf{\Pi}}_{\mathbf{k-1}}^{\mathbf{0},\hat{\mathbf{x}}_2,\hat{\mathbf{E}}}$, since its trend is very similar to the one of the condition number of $\hat{\mathbf{\Pi}}_{\mathbf{k-1}}^{\mathbf{0},\hat{\mathbf{x}}_1,\hat{\mathbf{E}}}$ for each method.

Finally, the condition and error measurements confirm that our technique shows very good improvements with respect to the monomial case. For high polynomial degrees, the orthonormal approach outperforms the inertial one. However, we recall that our procedure leads to a huge reduction in the overall computational cost as it does not depend on the local polynomial degree k.

4.3. Test 3: Badly-shaped polyhedrons and aligned faces in 3D

In the following, we analyse the three-dimensional case. Let $\Omega = (0, 1)^3$, we consider the problem (14) with constant coefficients $\boldsymbol{D} = \mathbf{I}$, $\gamma = 0$ and $\mathbf{b} = \mathbf{0}$, where we defined f and the non-homogeneous Dirichlet boundary condition in such a way the exact solution is the polynomial function of degree 6:

$$u(x_1, x_2, x_3) = 1.7 + 64x_1x_2x_3(1 - x_1)(1 - x_2)(1 - x_3).$$

In this experiment, we generate:

- a regular tetrahedral mesh (RTTM in short) to validate our procedures in the 3D case (Fig. 7(a));
- a generic polyhedral mesh (GPDM in short) made up mostly of badly-shaped polyhedrons and characterized by a copious number of aligned faces (Fig. 7(b)).

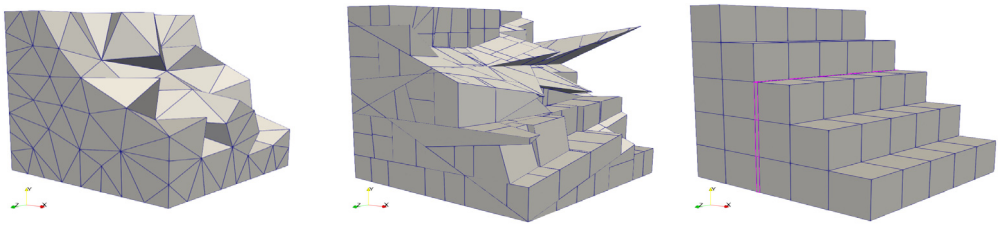

Fig. 7. Meshes used for Tests 3 and 4 clipped on the cubic domain $[0,1]^3$. Left: Tetrahedral mesh (RTTM). Centre: Polyhedral mesh (GPDM). Right: Collapsing polyhedrons (CCM_1).

Table 4
Properties of faces of meshes used in the Test 3 and in the Test 4.

	$\#\mathcal{F}_h$	N_v^f		Area			Diameter			Anisotropic ratio			Edge ratio		
		avg		min	avg	max	min	avg	max	min	avg	max	min	avg	max
RTTM	1330	3	f	7.8e−3	3.0e−2	6.8e−2	1.8e−1	3.3e−1	4.7e−1	1.0e+0	3.4e+0	1.2e+1	1.0e+0	1.6e+0	2.8e+0
			$\check{f}$	4.3e−1	4.3e−1	4.3e−1	1.0e+0	1.0e+0	1.0e+0	1.0e+0	1.0e+0	1.0e+0	1.0e+0	1.0e+0	1.0e+0
GPDM	2017	5.1	f	3.6e−7	1.2e−2	8.3e−2	1.9e−3	1.7e−1	7.9e−1	1.0e+0	3.5e+3	1.2e+6	1.0e+0	4.4e+1	4.4e+3
			$\check{f}$	4.3e−1	4.9e−1	6.1e−1	1.0e+0	1.0e+0	1.0e+0	1.0e+0	1.0e+0	1.0e+0	1.0e+0	2.6e+1	2.7e+3
CCM_1	535	4	f	4.0e−3	3.6e−2	4.0e−2	2.0e−1	2.7e−1	2.8e−1	1.0e+0	1.2e+1	1.0e+2	1.0e+0	2.0e+0	1.0e+1
			$\check{f}$	5.0e−1	5.0e−1	5.0e−1	1.0e+0	1.0e+0	1.0e+0	1.0e+0	1.0e+0	1.0e+0	1.0e+0	1.0e+0	1.0e+0
CCM_2	535	4	f	4.0e−4	3.6e−2	4.0e−2	2.0e−1	2.7e−1	2.8e−1	1.0e+0	1.1e+3	1.0e+4	1.0e+0	1.2e+1	1.0e+2
			$\check{f}$	5.0e−1	5.0e−1	5.0e−1	1.0e+0	1.0e+0	1.0e+0	1.0e+0	1.0e+0	1.0e+0	1.0e+0	1.0e+0	1.0e+0
CCM_3	535	4	f	4.0e−5	3.6e−2	4.0e−2	2.0e−1	2.7e−1	2.8e−1	1.0e+0	1.1e+5	1.0e+6	1.0e+0	1.1e+2	1.0e+3
			$\check{f}$	5.0e−1	5.0e−1	5.0e−1	1.0e+0	1.0e+0	1.0e+0	1.0e+0	1.0e+0	1.0e+0	1.0e+0	1.0e+0	1.0e+0

Table 5
Properties of bulks of meshes used in Test 3 and in Test 4.

	$\#\mathcal{T}_h$	N_v^E	N_e^E	N_f^E		Volume			Diameter			Anisotropic ratio			Face ratio		
		avg	avg	avg		min	avg	max	min	avg	max	min	avg	max	min	avg	max
RTTM	569	4	6	4	E	3.3e−4	1.8e−3	5.0e−3	1.8e−1	3.5e−1	4.7e−1	1.5e+0	1.0e+1	1.9e+2	1.1e+0	1.8e+0	3.5e+0
					$\hat{E}$	1.2e−1	1.2e−1	1.2e−1	1.0e+0	1.0e+0	1.0e+0	1.0e+0	1.0e+0	1.0e+0	1.0e+0	1.0e+0	1.0e+0
GPDM	308	20.5	30.6	12.1	E	6.7e−7	3.2e−3	6.2e−3	4.6e−2	3.2e−1	7.9e−1	1.4e+0	9.2e+0	4.2e+2	1.4e+0	1.8e+3	8.9e+4
					$\hat{E}$	1.2e−1	1.8e−1	2.2e−1	1.0e+0	1.0e+0	1.0e+0	1.0e+0	1.0e+0	1.0e+0	1.0e+0	1.7e+3	7.5e+4
CCM_1	150	8	12	6	E	8.0e−4	6.7e−3	8.0e−3	2.8e−1	3.3e−1	3.5e−1	1.0e+0	1.8e+1	1.0e+2	1.0e+0	2.5e+0	1.0e+1
					$\hat{E}$	1.9e−1	1.9e−1	1.9e−1	1.0e+0	1.0e+0	1.0e+0	1.0e+0	1.0e+0	1.0e+0	1.0e+0	1.0e+0	1.0e+0
CCM_2	150	8	12	6	E	8.0e−5	6.7e−3	8.0e−3	2.8e−1	3.4e−1	3.5e−1	1.0e+0	1.7e+3	1.0e+4	1.0e+0	1.8e+1	1.0e+2
					$\hat{E}$	1.9e−1	1.9e−1	1.9e−1	1.0e+0	1.0e+0	1.0e+0	1.0e+0	1.0e+0	1.0e+0	1.0e+0	1.0e+0	1.0e+0
CCM_3	150	8	12	6	E	8.0e−6	6.7e−3	8.0e−3	2.8e−1	3.4e−1	3.5e−1	1.0e+0	1.7e+5	1.0e+6	1.0e+0	1.7e+2	1.0e+3
					$\hat{E}$	1.9e−1	1.9e−1	1.9e−1	1.0e+0	1.0e+0	1.0e+0	1.0e+0	1.0e+0	1.0e+0	1.0e+0	1.0e+0	1.0e+0

The main geometric properties of the polyhedrons and of the polygonal faces belonging to these meshes are shown in Tables 4 and 5. More precisely, for the polyhedron elements we consider the volume, the diameter, the anisotropic ratio and the *face ratio*, i.e. the ratio between the highest and the smallest areas of the faces of the polyhedron. Instead, for the polygonal faces we measure the area, the diameter, the anisotropic ratio and the edge ratio. As in the 2D case, the application of F_E tends to uniform elements belonging to the same categories, as happens in the case of tetrahedrons. Moreover, we note that the face ratio of the mapped elements related to GPDM is not far from the face ratio of the original elements, since the map does not take into account the presence of aligned faces. However, we do not care about the geometric properties related to the faces of the mapped elements $\hat{E}$, since we never use them (see Remark 3.1).

We measure the performances of the different VEM approaches up to polynomial degree $k = 7$, as the dimension of the local and global matrices increase faster in the three-dimensional setting.

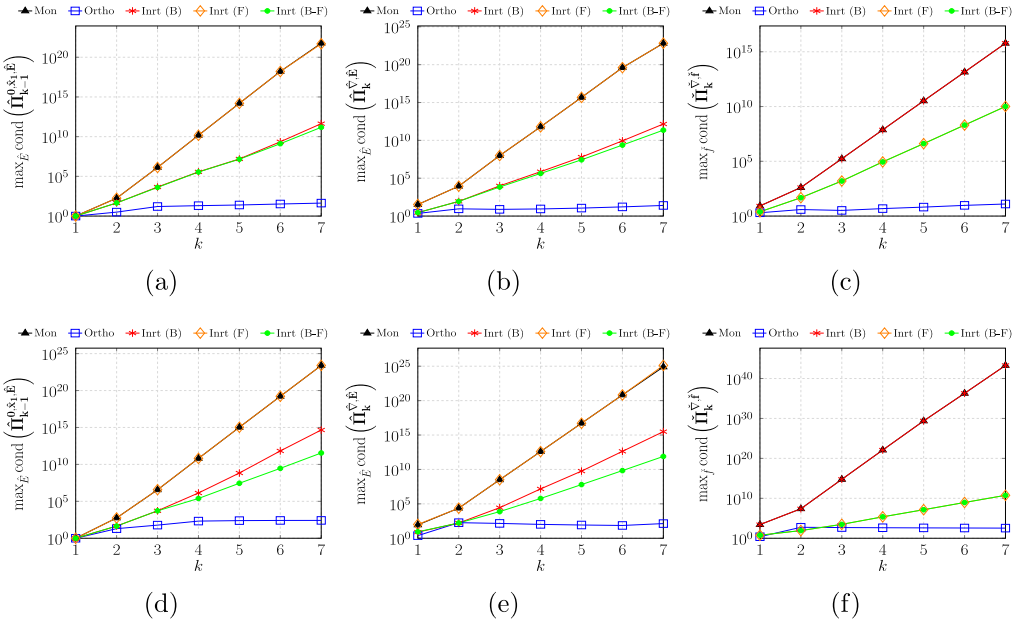

Fig. 8. Test 3: Behaviours of the worst condition numbers of both the 2D and the 3D local projection matrices among elements with respect to k. Top: RTTM. Bottom: GPDM.

Fig. 8 shows the behaviour of the condition numbers of the 2D and the 3D local projection matrices while varying the polynomial degree k. We omit the graphs reporting the behaviours of the condition numbers of $\hat{\mathbf{\Pi}}^{\mathbf{0},\hat{\mathbf{x}}_2,\hat{\mathbf{E}}}_{\mathbf{k-1}}$ and $\hat{\mathbf{\Pi}}^{\mathbf{0},\hat{\mathbf{x}}_3,\hat{\mathbf{E}}}_{\mathbf{k-1}}$ with respect to k, since these trends are very similar to the one of the condition number of $\hat{\mathbf{\Pi}}^{\mathbf{0},\hat{\mathbf{x}}_1,\hat{\mathbf{E}}}_{\mathbf{k-1}}$ for each method.

By looking at those figures, we can observe that by using the inertial approach (F), and thus by mapping only the faces of the elements, we improve just the condition numbers of the 2D local projection matrices, whereas the condition numbers of the 3D local projection matrices are comparable to the ones obtained with the standard monomial approach. For the same reason, the condition numbers of 2D local projection matrices related to the inertial approach (B) are in the same order of magnitude as the monomial ones. We observe that the condition numbers of the 3D local projection matrices in the inertial approach (B) differ from the ones related to the inertial approach (B-F) even if we use the same mapping for their bulks, because of the different contributions of the boundary integrals. Finally, we note that the condition numbers of 2D local projection matrices related to the Inrt (B-F) approach are equal to the ones obtained by resorting to the inertial approach (F), since the projectors are computed on the same faces in both cases.

Fig. 9 shows the trends of the condition number of the system matrix and of the errors (19) and (20) with respect to k. As expected from the local behaviour, the performances of the inertial approach (F) overlap the monomial one in both tests. On the other hand, the other two inertial approaches (B) and (B-F) lead to very good results in terms of the condition number of the global matrix. Moreover, we observe that the global performances of the (B-F) strategy are comparable and sometimes better than those obtained with the orthonormal approach in the case of the polyhedral mesh GPDM. Finally, we note that the errors related to both Inrt (B-F) and Ortho correctly decay to zero when $k = 6$, since the exact solution is a polynomial function of degree 6, whereas the errors related to the other approaches start to raise for $k \geq 5$.

In conclusion, the results show that mapping only the faces or only the bulks of elements of the mesh is not sufficient to obtain more reliable and accurate solutions. On the other hand, using the inertial approach (B-F) is very efficient from a computational point of view and leads to very high-quality results.

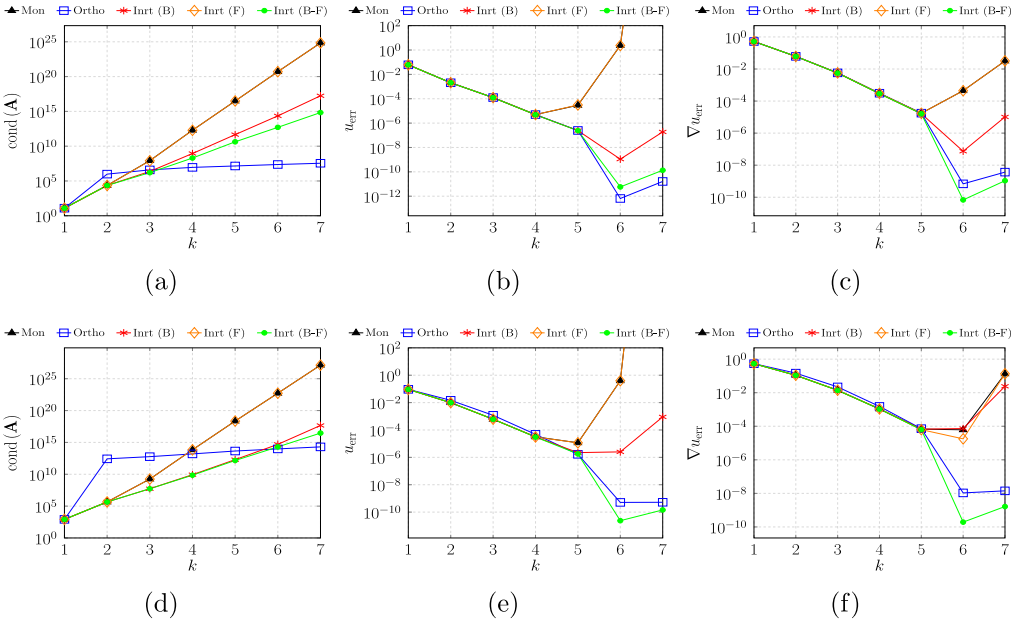

Fig. 9. Test 3: Behaviours of the condition number of the global system matrix and of errors (19) and (20) with respect to k. Top: RTTM. Bottom: GPDM.

4.4. Test 4: Collapsing polyhedrons

This experiment represents a natural extension of Test 2 to the 3D case. Thus, we consider on $\Omega = (0, 1)^3$ the advection–diffusion–reaction problem (14) with variable coefficients given by

$$\boldsymbol{D}(x_1, x_2, x_3) = \begin{bmatrix} 1 + x_2^2 + x_3^2 & -x_1x_2 & -x_1x_3 \\ -x_1x_2 & 1 + x_1^2 + x_3^2 & -x_2x_3 \\ -x_1x_3 & -x_2x_3 & 1 + x_1^2 + x_2^2 \end{bmatrix},$$

$$\mathbf{b}(x_1, x_2, x_3) = \begin{bmatrix} x_1 \\ x_2 \\ -2x_3 \end{bmatrix}, \quad \gamma(x_1, x_2, x_3) = x_1x_2x_3.$$

and we set f in such a way the exact solution is

$$u(x_1, x_2, x_3) = \sin(\pi x_1)\sin(\pi x_2)\sin(\pi x_3).$$

We further generate a sequence of three hexahedral meshes with cubic elements of edge length 0.2 with the exception of a central band made by two groups of hexahedrons, one of which (the purple band highlighted in Fig. 7(c)) is composed of hexahedrons whose volumes vary from $8 \cdot 10^{-4}$ in the first mesh CCM_1 to $8 \cdot 10^{-6}$ in the last mesh CCM_3 of the sequence as a consequence of the shrinkage performed along the x_1-direction. Fig. 7(c) shows a clip of the first mesh, while Tables 4 and 5 summarize the 2D and 3D geometric properties of the meshes CCM_i, $i \in \{1, 2, 3\}$.

Fig. 10 depicts the behaviour of the condition numbers of local projection matrices for the three meshes with respect to the polynomial degree k. For this particular test, we decide to plot the behaviour of the local condition number of all three local projection matrices $\hat{\boldsymbol{\Pi}}_{\mathbf{k-1}}^{\mathbf{0},\hat{\mathbf{x}}_\mathbf{i},\hat{\mathbf{E}}}$, with $i = 1, 2, 3$, to highlight the differences between the conditioning of the local projection matrices of the derivatives along the x_1-axis, i.e. the direction of the shrinkage, and the conditioning of $\hat{\boldsymbol{\Pi}}_{\mathbf{k-1}}^{\mathbf{0},\hat{\mathbf{x}}_\mathbf{i},\hat{\mathbf{E}}}$, with $i = 2, 3$.

As it happens for the 2D case, mapping only the faces with the (F) approach makes uniform the condition numbers of the 2D local projection matrices among meshes in the sequence. On the other hand, mapping only the bulks in the (B) approach does not make the condition numbers of the 3D local projection matrices independent of the

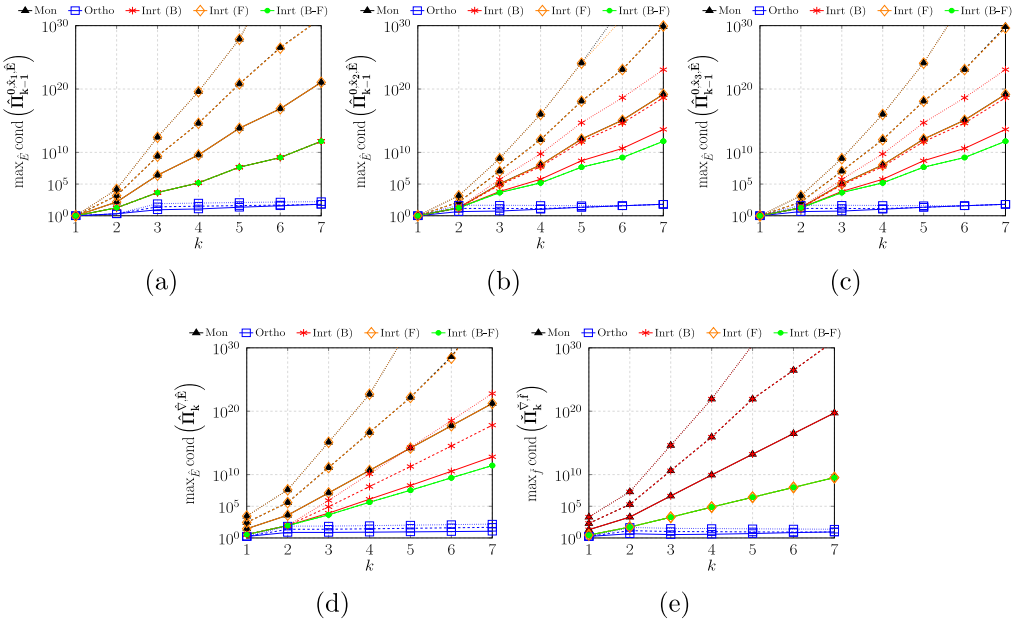

Fig. 10. Test 4: Behaviours of the worst condition numbers of both the 2D and the 3D local projection matrices among elements with respect to k. Solid lines: CCM_1. Dashed lines: CCM_2. Dotted lines: CCM_3.

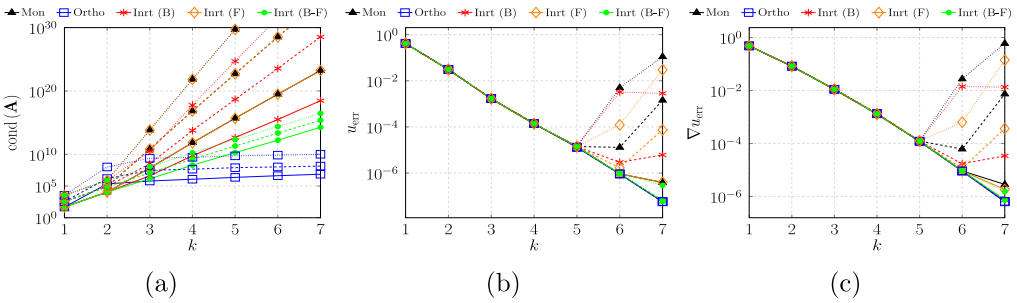

Fig. 11. Test 3: Behaviours of the condition number of the global system matrix and of errors (19) and (20) with respect to k. Solid lines: CCM_1. Dashed lines: CCM_2. Dotted lines: CCM_3.

mesh of the sequence since the boundary contributions depend on the actual mesh. Finally, mapping both faces and bulks with the inertial (B-F) approach makes the condition numbers of all local projection matrices approximately independent of the features of the central band.

To conclude the analysis, in Fig. 11 we show the global performances of all the aforementioned approaches in terms of the condition number of the global system matrix and of the errors (19) and (20). As concluded for the Test 3, the global performances of all the inertial approaches depend on the geometric properties of the original meshes of the sequence. Furthermore, the inertial approach (B-F) reveals to be more robust and more accurate than the monomial approach and it has a behaviour comparable to the one of the orthonormal approach, besides being the best advantageous choice from a computational point of view.

4.5. Test 5: A concave case

Now, we propose a simple test on a concave mesh, which is obtained by randomly agglomerating neighbouring elements of a starting triangular mesh that share a vertex. An example of the produced meshes is depicted in Fig. 12. In particular, in this test, the agglomeration process starts from a mesh obtained through the shrinkage

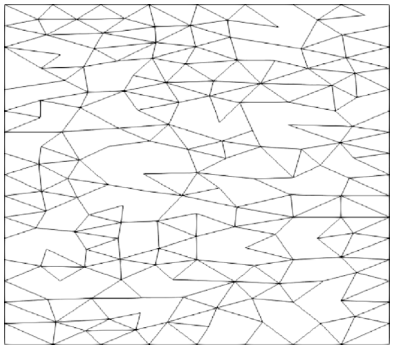

Fig. 12. Test 5: A concave mesh generated by the agglomeration procedure.

Table 6
Test 5: Examples of F_E mapping if E is a concave element.

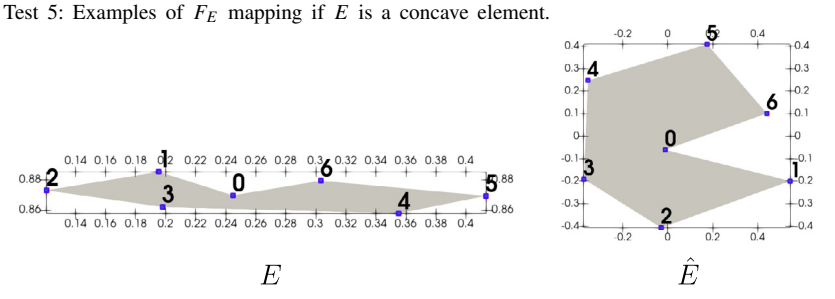

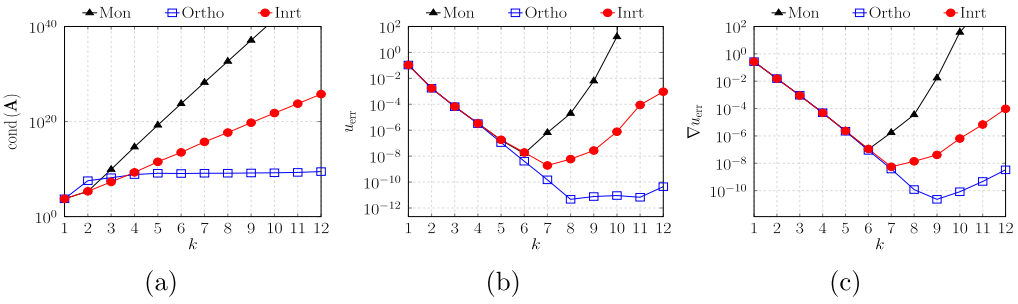

Fig. 13. Test 5: Behaviours of the condition numbers of the global system matrix and of errors (19), (20) with respect to k.

from $[0, 1] \times [0, 10]$ to $[0, 1] \times [0, 1]$ of a regular triangular mesh to create a more challenging test environment. The geometric properties of the resulting concave mesh CM are shown in Table 3, while an example of how our map acts on these concave elements is shown in Table 6. We highlight that the high aspect ratio which characterizes the original elements is mainly due to the initial shrinkage performed. Indeed, without such initial shrinkage, our original concave elements have an aspect ratio that scales like $O(1)$. Furthermore, we state that the proposed inertial strategy is mainly designed for the case of convex polytopes since the treatment of concave polytopes paves the way for a huge number of situations that we cannot analyse. Thus our considerations are limited to the concave case that we analyse here.

Now, we consider the elliptic problem presented in Section 4.2 to compare the performances of the aforementioned approaches. Fig. 13 illustrates the behaviour of the condition number of the global system matrix $\mathbf{A}$ and of errors (19) and (20) with respect to k and at the fixed mesh CM. Despite the presence of concave elements, also in this case we can observe that our strategy helps to strongly reduce the condition number of $\mathbf{A}$ with respect to the monomial approach by improving the reliability of the solution. Finally, we observe that, in this case, the orthonormal approach performs better than our strategy in terms of accuracy, while still being more demanding from a computational point of view.

4.6. The computational times

In this section, we compare the most cumbersome numerical experiments that we perform in both the 2D and 3D cases in terms of the computational time, namely the resolutions of the Poisson problem which exploit the highly-distorted hexagonal mesh HDHM (Fig. 1(a)) in Test 1 and the Polyhedral mesh GPDM (Fig. 7(b)) in Test 3. We consider the time required by each approach to perform all the tasks required to assemble the local stiffness matrix for all the elements of $\mathcal{T}_h$, i.e. the computation of the local projectors, the orthogonalization step in the Ortho approach, the mapping of the elements and the changing of variable in the integrals (see (16)) in the Inrt approach. We measure only the time required for these operations since they represent the only differences in our code among the aforementioned approaches.

Fig. 14 displays the behaviours of the ratio r_{time} between the time required by the Inrt and the Ortho approach with respect to the time related to the monomial strategy for different values of the polynomial degree k for both the two-dimensional HDHM mesh and the three-dimensional GPDM mesh. We further report on the top of the figure the number of the DOFs N^{dof} to understand the dimension of the problem. In the 3D case, for the sake of brevity, we report only the Inrt (B-F) approach, since it is the most accurate and the most expensive from a computational point of view among the three-dimensional inertial strategies.

Firstly, we observe that $r_{\text{time}} \geq 1$ for each approach and each polynomial degree k, since each approach requires at least all the computations required also for the monomial approach. Furthermore, we note that we include the time needed to compute the mapped elements for the Inrt approach for each k even if these operations could be performed just once at all for all the polynomial degrees since they are independent of k. This property can help to strongly reduce the overall cost, for example, related to a p-method.

In Fig. 14 we can observe that the computational times reflect our previous theoretical discussion: the additional cost required by the Inrt approach for the mapping becomes negligible for the higher values of the polynomial degrees (or of the number of DOFs) by leading to a value of the time ratio that is approximately equal to 1 for the higher values of the polynomial degrees. On the other hand, the additional cost related to the Ortho approach becomes higher and higher with k.

5. Conclusions

One of the main features of the Virtual Element Method is the possibility to use very complex geometries, but the use of the classical scaled monomial basis in its construction generally leads to very low-quality results in the presence of badly-shaped polytopes and for high polynomial degrees.

In this paper, we propose a new procedure to build a polynomial basis on polytopes to mitigate the ill-conditioning of the local projection matrices and of the global system matrix with a computational complexity that depends only on the geometric dimension of the problem ($d = 2$ or 3) and on the number of faces in 3D.

Throughout different numerical experiments of increasing complexity in 2D and 3D cases, we observe that recomputing the scaled monomial basis on more well-shaped polytopes leads to obtain an acceptable well-conditioned polynomial basis and, consequently, a more reliable solution. We highlight the need of defining both the 2D and 3D polynomial bases on well-shaped polytopes in the 3D case in order to improve the local and global performances with respect to the use of the standard scaled monomial basis.

Finally, the proposed approach has proved to have reasonable and, most of the time, comparable results from a practical point of view with respect to the use of a local orthonormal polynomial basis, while being less expensive from a computational point of view.

Acknowledgements

The author S.B. kindly acknowledges partial financial support provided by PRIN project “Advanced polyhedral discretizations of heterogeneous PDEs for multiphysics problems” (No. 20204LN5N5_003) and by PNRR M4C2 project of CN00000013 National Centre for HPC, Big Data and Quantum Computing (HPC) (CUP: E13C22000990001). The author G.T. kindly acknowledges financial support provided by the MIUR programme “Programma Operativo Nazionale Ricerca e Innovazione 2014 - 2020” (D.M. 1061/2021, CUP: E11B21006490005). F.V. kindly acknowledges partial financial support provided by INdAM-GNCS (CUP: E53C22001930001). The authors are members of the Italian INdAM-GNCS research group.

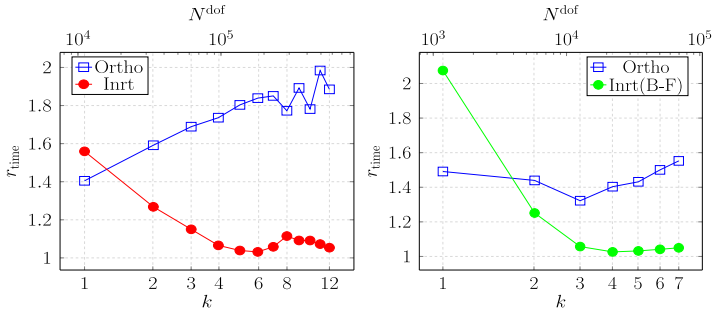

Fig. 14. Test 5: Behaviours of ratio r_{time} between the time required by the Inrt and from the Ortho approach with respect to the time related to the monomial strategy. Left: HDHM (2D). Right: GPDM (3D).

References

[1] B. Ahmad, A. Alsaedi, F. Brezzi, L. Marini, A. Russo, Equivalent projectors for virtual element methods, Comput. Math. Appl. 66 (3) (2013) 376–391.

[2] P.F. Antonietti, S. Berrone, A. Borio, A. D'Auria, M. Verani, S. Weisser, Anisotropic a posteriori error estimate for the virtual element method, IMA J. Numer. Anal. 42 (2) (2021) 1273–1312, [Online]. Available: https://doi.org/10.1093/imanum/drab001.

[3] L. Beirão da Veiga, F. Brezzi, A. Cangiani, G. Manzini, A. Russo, Basic principles of virtual element methods, Math. Models Methods Appl. Sci. 23 (01) (2013) 199–214.

[4] L. Beirão da Veiga, F. Brezzi, L. Marini, A. Russo, The hitchhiker's guide to the virtual element method, Math. Models Methods Appl. Sci. 24 (8) (2014) 1541–1573.

[5] L. Beirão da Veiga, F. Brezzi, L.D. Marini, A. Russo, Virtual element methods for general second order elliptic problems on polygonal meshes, 2016, pp. 729–750.

[6] S. Berrone, A. Borio, Orthogonal polynomials in badly shaped polygonal elements for the virtual element method, Finite Elem. Anal. Des. 129 (2017) 14–31.

[7] F. Dassi, L. Mascotto, Exploring high-order three dimensional virtual elements: Bases and stabilizations, Comput. Math. Appl. 75 (9) (2018) 3379–3401, [Online]. Available: https://www.sciencedirect.com/science/article/pii/S0898122118300786.

[8] D.A. Di Pietro, A. Ern, A hybrid high-order locking-free method for linear elasticity on general meshes, Comput. Methods Appl. Mech. Engrg. 283 (2015) 1–21, [Online]. Available: https://www.sciencedirect.com/science/article/pii/S0045782514003181.

[9] A. Ern, F. Hédin, G. Pichot, N. Pignet, Hybrid high-order methods for flow simulations in extremely large discrete fracture networks, 2021, [Online]. Available: https://hal.inria.fr/hal-03480570, working paper or preprint.

[10] L. Mascotto, Ill-conditioning in the virtual element method: stabilizations and bases, 2017, arXiv:1705.10581.

[11] T. Sorgente, S. Biasotti, G. Manzini, M. Spagnuolo, Polyhedral mesh quality indicator for the virtual element method, Comput. Math. Appl. 114 (2022) 151–160, [Online]. Available: https://www.sciencedirect.com/science/article/pii/S0898122122001390.

[12] T. Sorgente, S. Biasotti, G. Manzini, M. Spagnuolo, The role of mesh quality and mesh quality indicators in the virtual element method, Adv. Comput. Math. 48 (1) (2022) [Online]. Available: https://doi.org/10.1007/s10444-021-09913-3.